ZnCo$_2$O$_4$/g-C$_3$N$_4$/Cu nanocomposite as a new efficient and recyclable heterogeneous photocatalyst with enhanced photocatalytic activity towards the Metronidazole degradation under the solar light irradiation

Roya Jahanshahi,[a] Alieh Mohammadi,[b] Mohammadreza Doosti,[b] Sara Sobhani,[a] José Miguel Sansano[c]*

AUTHOR ADDRESSES:

[a] Department of Chemistry, College of Sciences, University of Birjand, Birjand, Iran, email: ssobhani@birjand.ac.ir, sobhanisara@yahoo.com.

[b] Department of Civil Engineering, Faculty of Engineering, University of Birjand, Birjand, Iran, email: mdoosti@birjand.ac.ir

[c] Departamento de Química Orgánica, Facultad de Ciencias, Centro de Innovación en Química Avanzada (ORFEO-CINQA) and Instituto de Síntesis Orgánica (ISO), Universidad de Alicante, Apdo. 99, 03080-Alicante, Spain.

ABSTRACT

In the present study, $ZnCo_2O_4/g\text{-}C_3N_4/Cu$ is synthesized as a new and highly effectual solar-light-driven heterogeneous photocatalyst. The prepared photocatalyst is characterized using FT-IR, XRD, XPS, DRS, FESEM, TEM, EDS, and elemental mapping techniques. The performance of $ZnCo_2O_4/g\text{-}C_3N_4/Cu$ is studied towards the Metronidazole (MNZ) degradation under the solar light radiation. The kinetics of MNZ degradation and efficacy of the operational parameters comprising the initial MNZ amount (10–30 mg L^{-1}), photocatalyst dosage (0.005–0.05 g L^{-1}), pH (3–11), and contact time (5–30 min) on the MNZ degradation process are investigated. Surprisingly, the $ZnCo_2O_4/g\text{-}C_3N_4/Cu$ nanocomposite present a privileged photocatalytic performance towards the MNZ degradation under solar light irradiation. The enhanced photocatalytic activity of this photocatalyst can be attributed to the synergistic optical effects between $ZnCo_2O_4$, $g\text{-}C_3N_4$, and Cu. The value of the band gap energy for $ZnCo_2O_4/g\text{-}C_3N_4/Cu$ is estimated to be 2.3 eV based on the Tauc plot of $(\alpha h \nu)^2$ *vs.* hν. The radical quenching experiments confirm that the superoxide radicals and holes are the principal active species in the photocatalytic degradation of MNZ, whereas the hydroxyl radicals have no major role in such a degredation. The as-prepared catalyst is simply isolated and recycled for at least eight runs without noticeable loss of efficiency. Using the natural sunlight source, applying very low amount of the photocatalyst, neutrality of the reaction medium, short reaction time, high efficiency of the degradation procedure, utilizing air as the oxidant, low operational costs and easy to recover and reuse of the catalyst are the significant highlights of the present method. It is supposed that this study can be a step forward in creating an effective photocatalytic system in the treatment of a wide range of contaminated aquatic environments.

KEYWORDS: Photocatalysis; Metronidazole; Heterogeneous catalysis; Solar light; Wastewater treatment

INTRODUCTION

In recent years, Earth's life has been further threatened by the entrance of harmful residues of the pharmaceuticals in the aqueous environment. As the most commonly used pharmaceuticals, antibiotics, that play an imperative role in the prevention and treatment of infections, considered as growing pollutants that required a specific attention.[1] Most of the antibiotics could not be metabolized completely in the body and have low biodegradability in nature, which causes many challenges in their elimination through conventional wastewater treatments.[2] Therefore, there is a critical need to develop the effectual methodologies for the mineralization of these pollutants from wastewater.[3,4] So far, several techniques have been reported for removing antibiotics from effluents, including the coagulation-flotation,[5] membrane filtration,[6] ion exchange processes,[7] adsorption,[8] chlorination processes,[9] reverse osmosis,[10] various advanced oxidation processes (AOPs),[11] etc. Among these methods, AOPs have been found to be predominantly efficient, owing to have the potential for complete degradation of pollutants compared with almost all of the alternative procedures.[12,13] In this line, heterogeneous semiconductor photocatalysis, as one of the most well-known AOP methods, has attracted intense attention as a low-cost, versatile, eco-benign, and sustainable method.[14,15] In 21st century, solar energy has drawn tremendous attention as a renewable, abundant, safe, green, and cheap energy source, which can effectually promote the photocatalytic processes through an eco-friendly manner.[16-18]

Graphitic carbon nitride (g-C_3N_4), which is a metal-free polymeric semiconductor with the narrow band gap energy (2.73 eV), appropriate visible-light response ($\lambda < 460$ nm), ease of preparation,

64 nontoxicity, low cost and chemical and thermal stability, has attracted enormous interest in the

65 area of the environmental remediation.[19,20] However, a problem that has severely hampered the

66 photocatalytic efficiency of g-C_3N_4 is the fast recombination rate of the photo-excited electron-

67 hole pairs in its structure.[21,22] One of the most operational techniques for improving the visible-

68 light harvesting capacity of g-C_3N_4 is the incorporation of other metal oxide semiconductors with

69 g-C_3N_4 to prepare composite photocatalysts.[23,24]

70 $ZnCo_2O_4$ as an environmentally benign, cost-effective and efficient transition bimetallic oxide is

71 amongst the most promising materials for numerous technological and environmental

72 applications.[25,26] It has found to be an ideal candidate for constructing an effective heterojunction

73 with other semiconductors.[27] $ZnCo_2O_4$ with the large absorption range (200–800 nm), have

74 particular optoelectronic properties that are beneficial for photocatalytic applications under solar

75 irradiation.[28] Furthermore, owing to its special crystal structure, as well as the synergistic effects

76 of its constituent metals, $ZnCo_2O_4$ shows superior electron conductivity and photo-electrochemical

77 stability compared with single metal oxides ZnO and Co_3O_4.[29,30] Fascinatingly, the band edges of

78 $ZnCo_2O_4$ and g-C_3N_4 could match well with each other and the fabricated heterojunction

79 comprising of these two semiconductors can repress the recombination speed of the photo-excited

80 electron/hole pairs, which leads to enhance visible light absorption potential.[25]

81 It is worthy of note that the combination of noble metal nanoparticles (NPs) with the photocatalytic

82 systems can significantly improve the efficacy of the process, especially under the visible light

83 illumination.[31-33] Among the noble metal used for this goal, copper NPs have attracted growing

84 interest in the photocatalytic processes due to have low-cost, earth-abundant, non-toxicity, and

85 stability.[34,35] Incorporation of Cu NPs to the photocatalytic system effectually increases the

86 separation ability of the photo induced electron/hole pairs, which subsequently improves the

87 visible-light photocatalytic capability of the photocatalyst.[31-33]

88 Inspired by these facts and following our persistent research interest in the development of new

89 photocatalytic systems to operate under mild conditions,[36,37] herein, we synthesized the

90 $ZnCo_2O_4/g-C_3N_4/Cu$ nanocomposite as a new, efficient and recyclable heterogeneous sunlight-

91 driven photocatalyst. It was fully characterized by different methods. The photocatalytic

92 performance of $ZnCo_2O_4/g-C_3N_4/Cu$ was well assessed towards the Metronidazole (MNZ)

93 degradation under the solar light illumination.

94

RESULTS AND DISCUSSION

Synthesis and characterization of $ZnCo_2O_4/g-C_3N_4/Cu$

97 Scheme 1 shows the overall multi-step synthetic procedure of $ZnCo_2O_4/g-C_3N_4/Cu$

98 nanocomposite. At first, the consecutive polymerization and liquid exfoliation processes were

99 performed to prepare the $g-C_3N_4$ nanosheets (NSs). Then, the freshly obtained $g-C_3N_4$ NSs was

100 added to an alkaline mixture of $Zn(NO_3)_2 \cdot 6H_2O$ and $Co(NO_3)_2 \cdot 6H_2O$, and refluxed. The resulting

101 pristine $ZnCo_2O_4/g-C_3N_4$ was calcined at 350 °C, before the adsorption of reduced $Cu(OAc)_2$ on its

102 surface and afforded the desired $ZnCo_2O_4/g-C_3N_4/Cu$. The freshly prepared $ZnCo_2O_4/g-C_3N_4/Cu$

103 was fully characterized *via* a collection of various techniques.
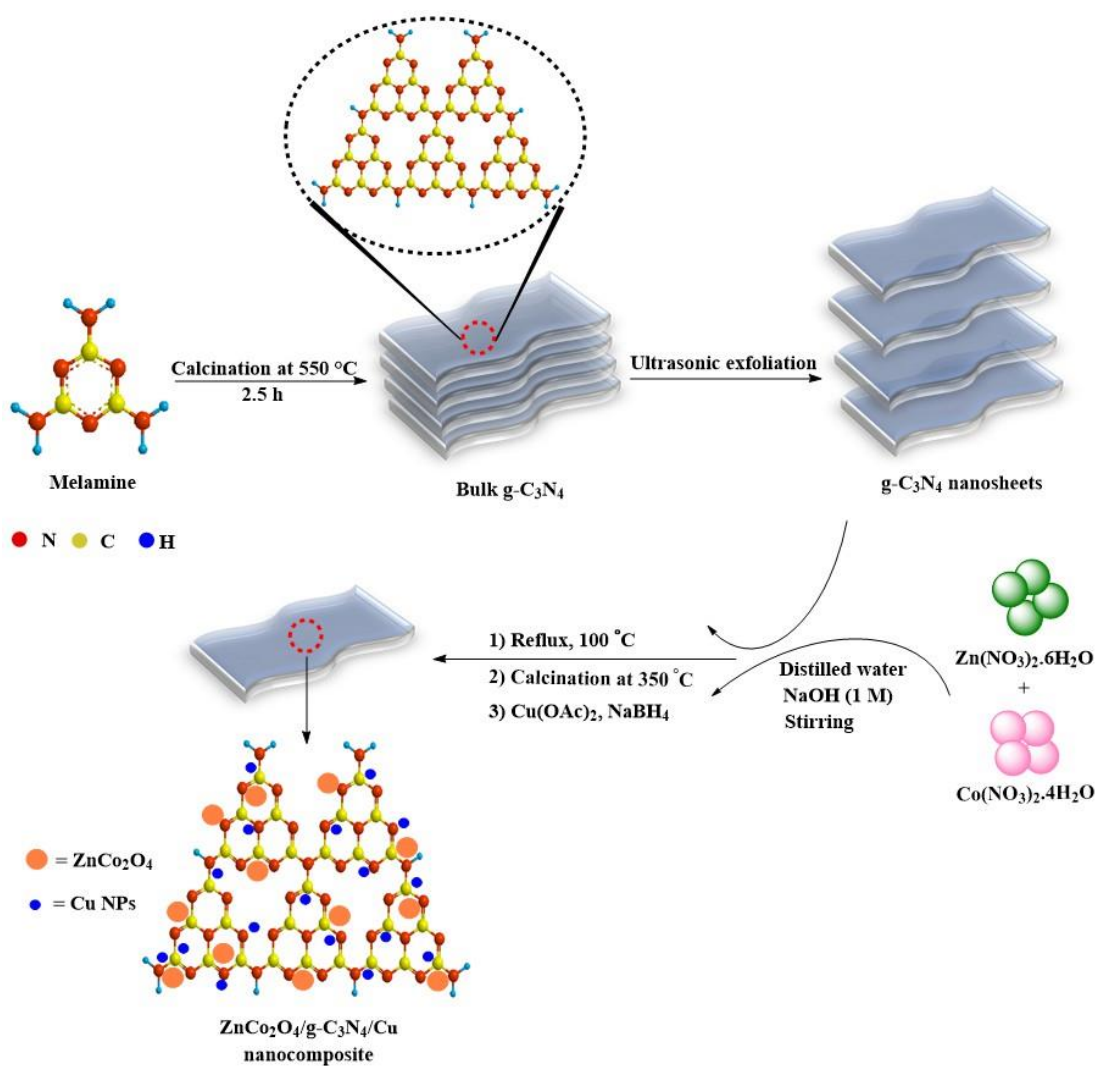
Scheme 1. Synthesis of ZnCo$_2$O$_4$/g-C$_3$N$_4$/Cu nanocomposite.

Figure 1 shown the FT-IR spectra of g-C$_3$N$_4$ and ZnCo$_2$O$_4$/g-C$_3$N$_4$/Cu. As indicated in the FT-IR spectrum of g-C$_3$N$_4$ (Figure 1a), a sharp adsorption band appearing around 807 cm^{-1} could be corresponded to breathing modes of triazine groups. The indicative adsorption bands relating to C=N and C–N stretching vibrations, are presented at around 1200–1650 cm^{-1}. Moreover, the broad adsorption band at about 3000–3400 cm^{-1} was ascribed to the stretching vibration frequencies of -NH bonds and the adsorbed water molecules on the catalyst surface. FT-IR spectrum of

113 ZnCo$_2$O$_4$/g-C$_3$N$_4$/Cu is depicted in Figure 1b. As illustrated, the presence of g-C$_3$N$_4$ characteristic

114 absorption bands along with the appearance of a new distinct absorption band at 638 cm^{-1}, which

115 is consigned to stretching modes of Co-O bond, certified the successful preparation and strong

116 stability of the catalyst.

117
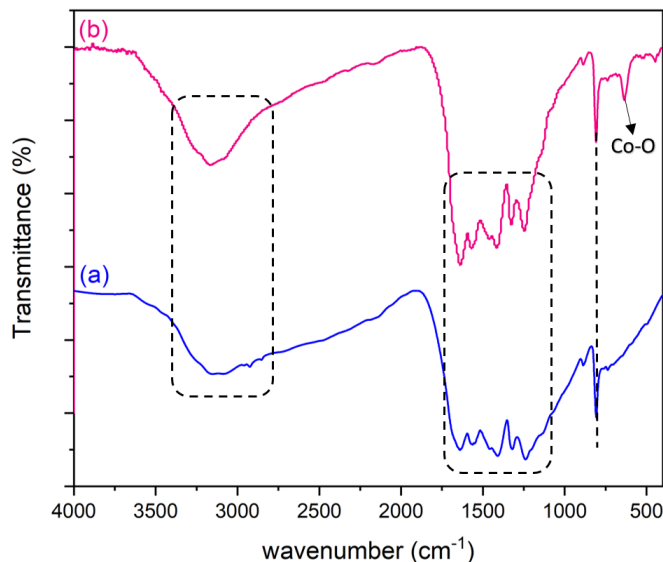
Figure 1. FT-IR spectra of (a) g-C$_3$N$_4$ and (b) ZnCo$_2$O$_4$/g-C$_3$N$_4$/Cu.

120

121 Electronic properties and elemental composition of ZnCo$_2$O$_4$/g-C$_3$N$_4$/Cu were probed *via* the XPS

122 analysis (Figure 2). The peaks relating to C, O, N, Co, Zn, and Cu elements can be evidently

123 detected in the XPS plot of the photocatalyst (Figure 2a). Figure 2b disclosed four characteristic

124 peaks in the high-resolution XPS spectrum of C 1s. The signals observed at 284.5, 285.8, 287.6

125 and 288.8 eV are assigned to the adventitious C-C bonds, sp^2 carbons in the C-N-C, N=C–(N)$_2$,

126 and N=C(N)–NH$_2$ and N=C(N)–NH, respectively. As shown in Figure 2c, the high-resolution XPS

127 spectra of O 1s revealed three peaks at 530.4, 531.6 eV (both indexed to the crystal lattice oxygen

128   atoms) and 533.2 eV (indexed to the adsorbed O_2 and H_2O molecules on the catalyst surface). The

129   high resolution of N 1s spectrum (Figure 2d) showed three indicative peaks at 398.3, 399.4, and

130   400.7 eV, belonged in turn to the sp^2 nitrogen atoms (C-N=C), sp^3 nitrogen atoms (H-N-C_3) and

131   amino groups (C-NH_x). Figure 2e indicates the signal peaks at 1021.0 and 1043.9 eV, which are

132   the characteristics of Zn $2p_{3/2}$ and Zn $2p_{1/2}$ in Zn^{2+}, respectively. As can be seen in Figure 2f, the

133   peaks at 779.8 eV (Co $2p_{3/2}$) and 795.0 eV (Co $2p_{1/2}$) are identified as Co^{3+}, and peaks at 781.9 eV

134   (Co $2p_{3/2}$) and 796.6 eV (Co $2p_{1/2}$) are ascribed to the Co^{2+} species. Two other peaks at 785.3 and

135   800.0 are allocated to the shake-up satellites, which further elucidating the existence of multivalent

136   cobalt. In the XPS spectrum of Cu (Figure 2g), the presence of binding energies at 932.5 eV (Cu

137    $2p_{3/2}$) and 952.2 eV (Cu $2p_{1/2}$) are the typical characteristics of Cu with zero oxidation state.

138   Meanwhile, the indicative peaks of Cu $2p_{3/2}$ at 934.3 and the peaks of Cu $2p_{1/2}$ located at 954.0 are

139   ascribed to Cu^{1+} in the catalyst. The two minor peaks positioned at 936.3 and 955.7 eV are related

140   to Cu(II) $2p_{3/2}$ and Cu(II) $2p_{1/2}$, respectively. Furthermore, two little satellite peaks are located at
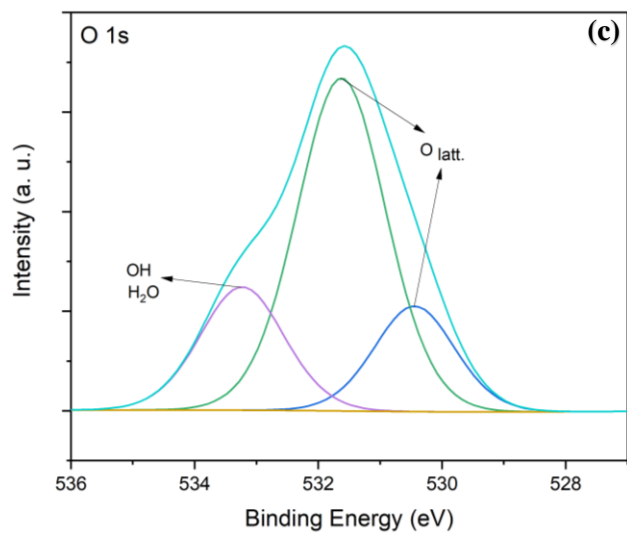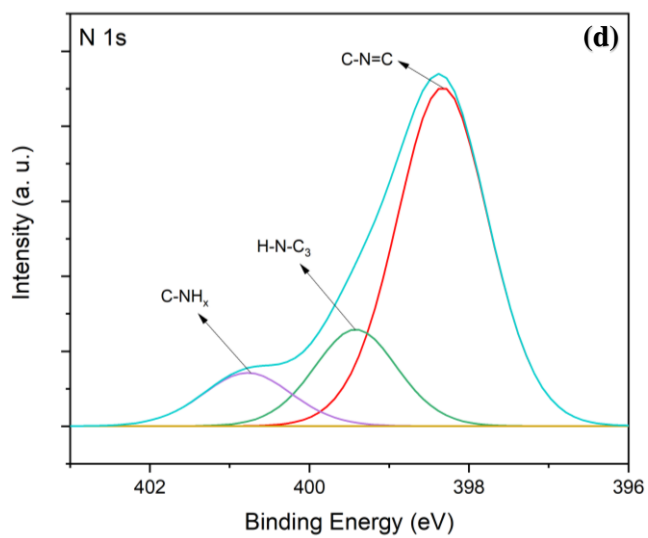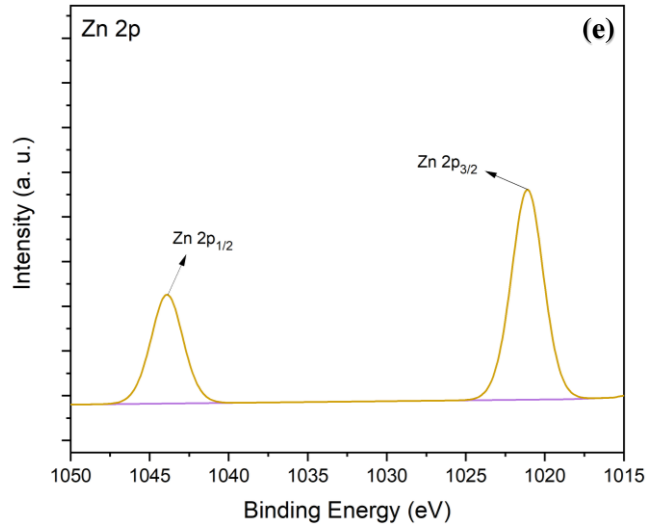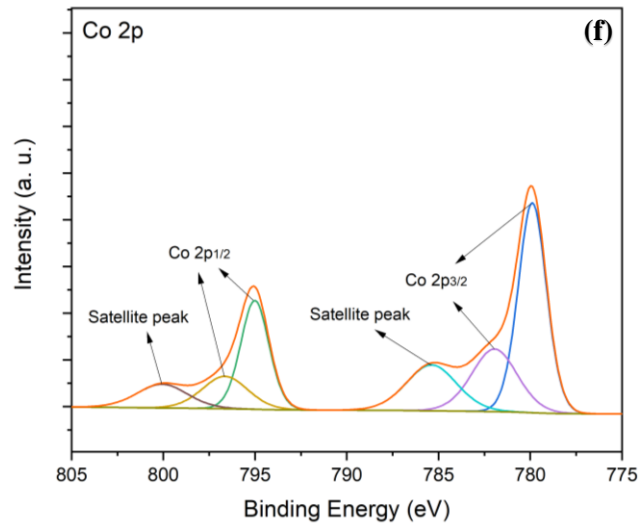
141   940.8 and 943.5 eV.

142

143

144
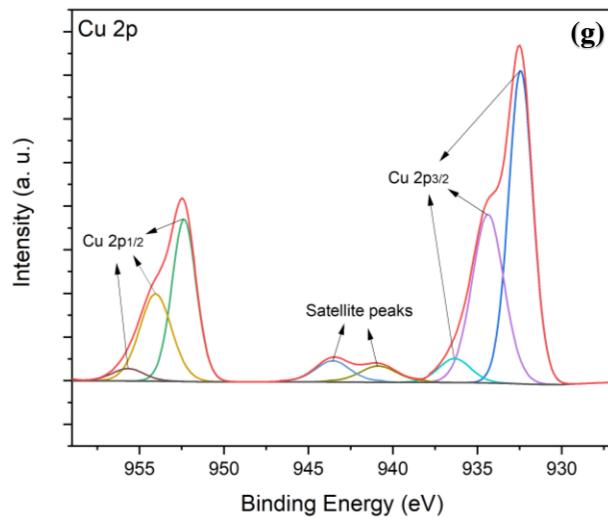

145

146

9
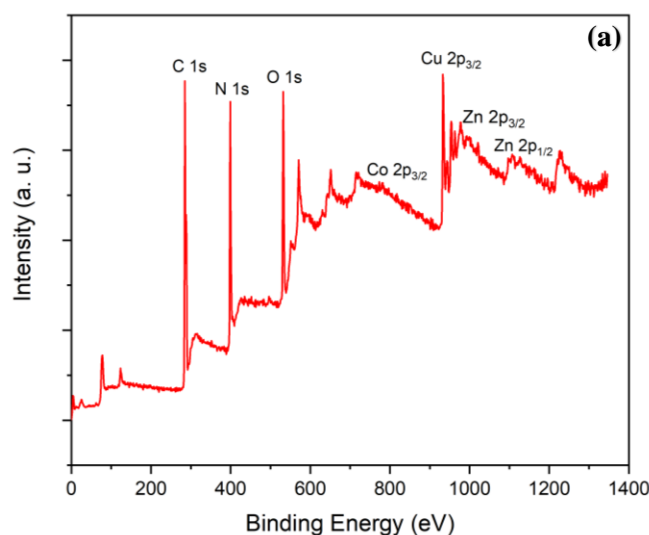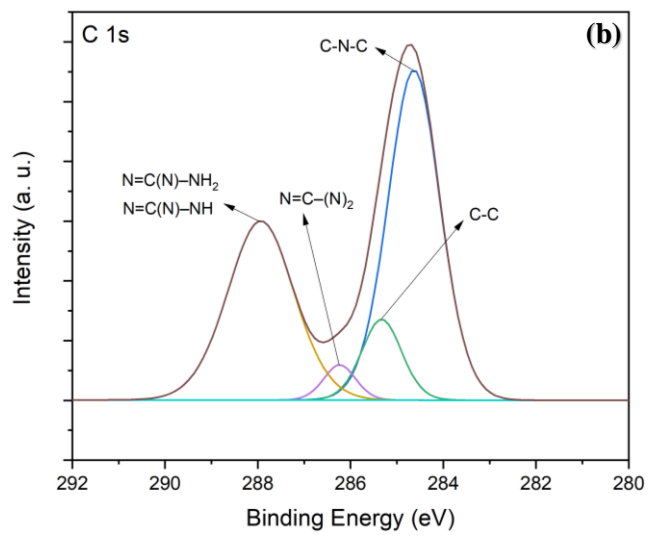
147

148

149

150 **Figure 2.** (a) XPS analysis of $ZnCo_2O_4/g-C_3N_4/Cu$, (b) C 1s, (c) O 1s, (d) N 1s, (e) Zn 2p, (f) Co

151 2p and (g) Cu 2p.

152

153 XRD analysis of $ZnCo_2O_4/g-C_3N_4$ and $ZnCo_2O_4/g-C_3N_4/Cu$ were performed to understand the

154 structural properties of the synthesized photocatalyst (Figure 3). As shown in Figure 3 (a and b),

155 signals at 13.1° and 27.3° are assigned to 1 0 0 and 0 0 2 crystal planes of $g-C_3N_4$ (JCPDS 87-

156 1526),[38] respectively. Furthermore, the indicative diffraction peaks at 31.2°, 36.6°, 44.7°, 59.2°

157 and 65.1° (2θ) are corresponded to the 2 2 0, 3 1 1, 4 0 0, 5 1 1 and 4 4 0 crystal planes of $ZnCo_2O_4$,

158 respectively, which are well consistent with the cubic spinel structure (JCPDS 23-1390)[39] (Figure

159 3 a and b). In the XRD pattern of $ZnCo_2O_4/g-C_3N_4/Cu$ (Figure 3b), the appearance of diffraction

160 peaks at 2θ ° = 43.3 °, 50.4 °, 74.1 °, which was indexed to the 1 1 1, 2 0 0 and 2 2 0 reflection

161 planes, (JCPDS 04-0836)[40] respectively, confirmed the presence of or Cu NPs in the composite.
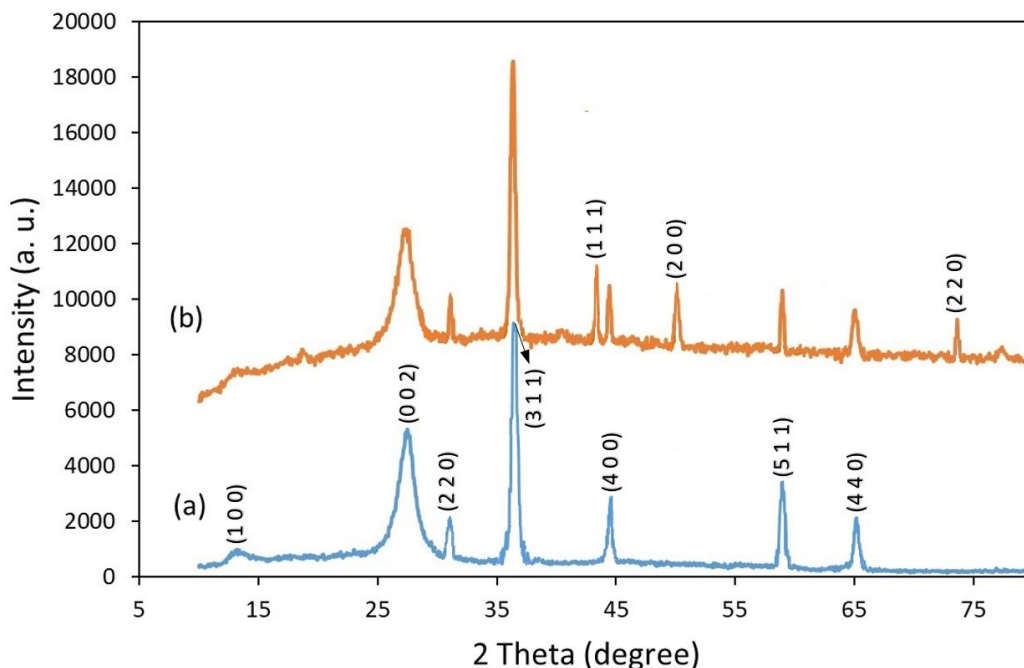
162

163 **Figure 3.** XRD patterns of (a) $ZnCo_2O_4/g-C_3N_4$ and (b) $ZnCo_2O_4/g-C_3N_4/Cu$.

164   The light absorption characteristics of the synthesized photocatalyst were investigated using the

165   UV-vis DRS technique. As it is apparent in Figure 4, the $ZnCo_2O_4/g$-C_3N_4/Cu photocatalyst

166   demonstrated a strong absorption in 200-800 region. The ability of this photocatalyst to absorb

167   both UV and visible light improves its photocatalytic performance in the solar light, which contains

168   a small portion of UV light and the most of it is composed of visible light. The value of the band

169   gap energy for $ZnCo_2O_4/g$-C_3N_4/Cu was estimated to be 2.3 eV based on the Tauc plot of $(\alpha h v)^2$

170   *vs.* hv (Figure 5), which affirmed the high ability of the photocatalyst to boost the separation

171   capacity of the photo-induced electron-hole pairs and develops the solar light photocatalytic
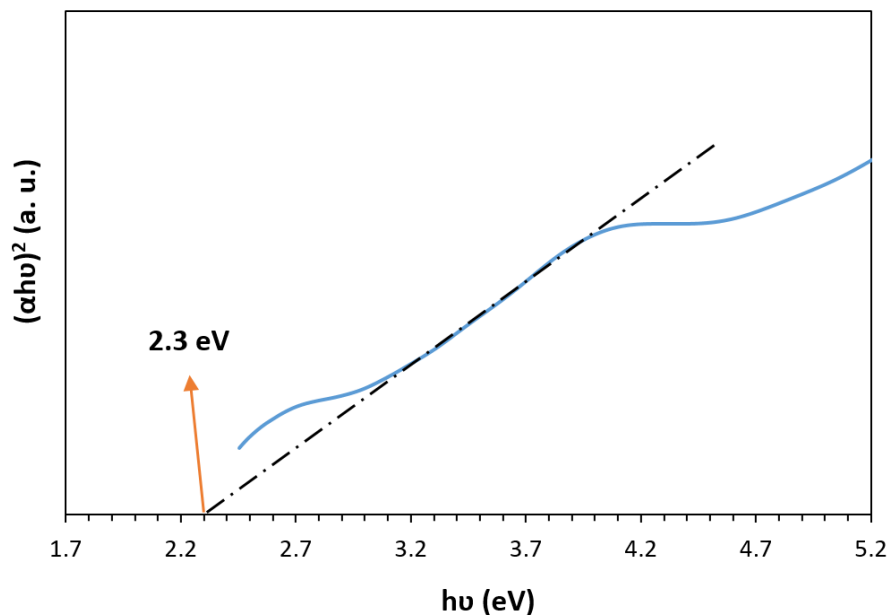
172   performance.

173

174
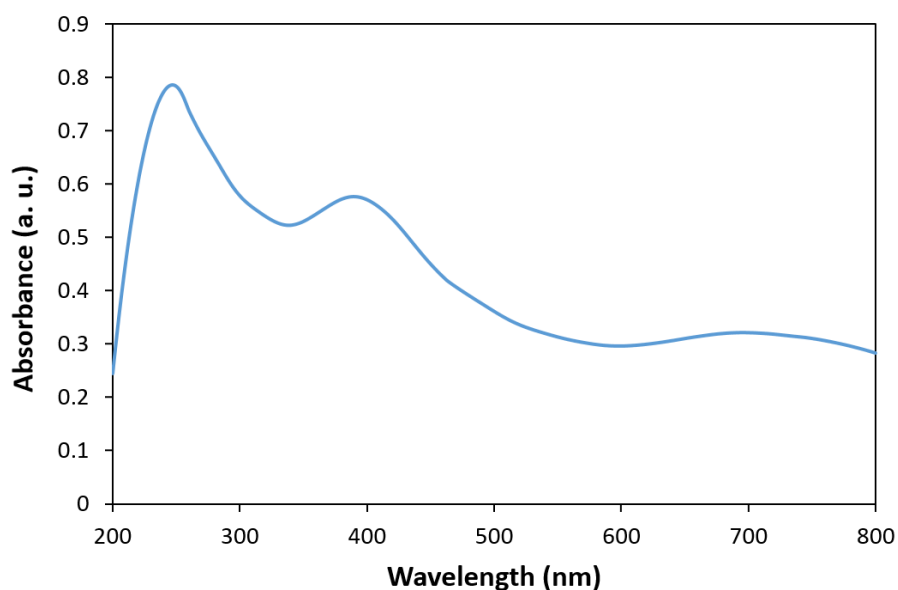
Figure 4. UV-vis DRS of $ZnCo_2O_4/g$-C_3N_4/Cu.

176

Figure 5. Tauc plot of $ZnCo_2O_4/g$-C_3N_4/Cu for the estimation of band gap energy.

FESEM and TEM were carried out to determine the morphological properties of $ZnCo_2O_4/g$-C_3N_4/Cu (Figure 6). Obviously, the sheet-like structure of g-C_3N_4 and the cubic structure of $ZnCo_2O_4$ can be seen (Figure a-c). The mean size of $ZnCo_2O_4$ particles was measured to be between 25 and 40 nm (Figure 6c). The lattice fringe observed at about 0.182 nm was ascribed to the 2 0 0 plane in Cu NPs (Figure 6d).

13

187
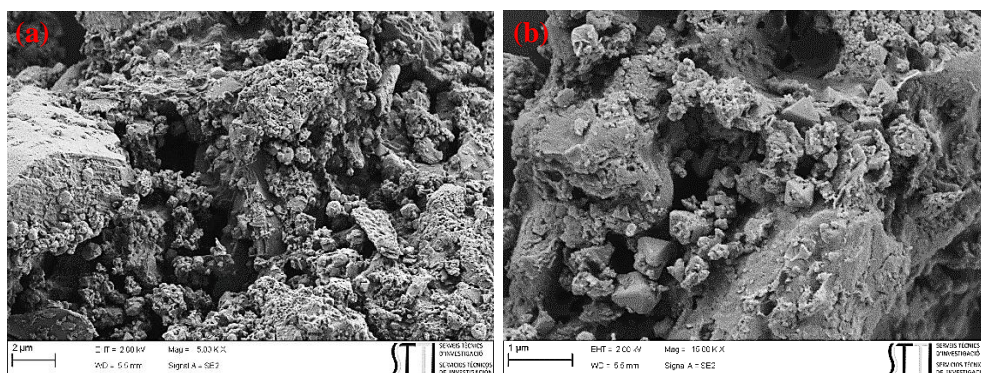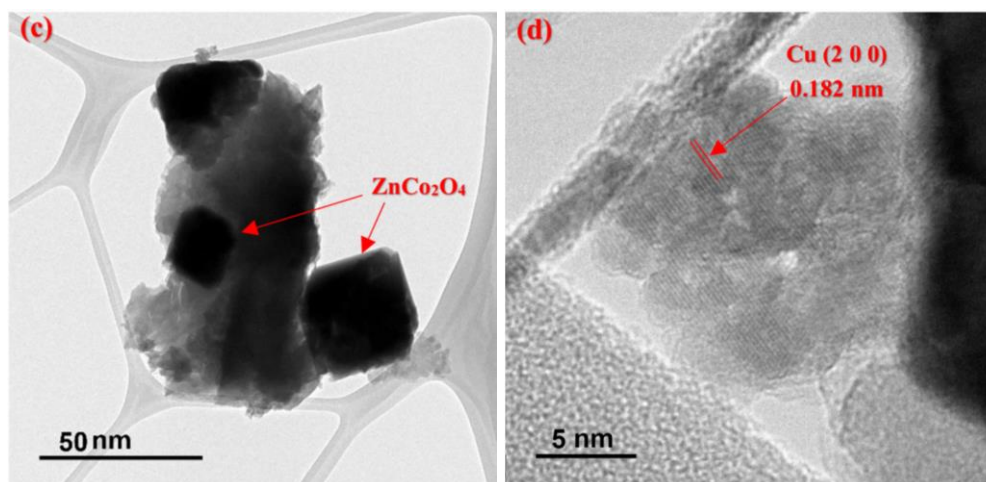
Figure 6. (a, b) FESEM images of $ZnCo_2O_4/g$-C_3N_4/Cu and (c, d) TEM images of $ZnCo_2O_4/g$-C_3N_4/Cu.

EDS analysis of the $ZnCo_2O_4/g$-C_3N_4/Cu verified the presence of O, N, C, Zn, Co and Cu elements through their consistent signals, which is another evidence to confirm the successful synthesis of the catalyst (Figure 7a). Besides, the elemental mapping analysis was done for probing the homogeneity of the elemental compositions in the $ZnCo_2O_4/g$-C_3N_4/Cu (Figure 7b-h). As can be seen in the images, the simultaneous presence of O, N, C, Zn, Co and Cu elements in association with their uniform distribution over the catalyst surface were well approved.
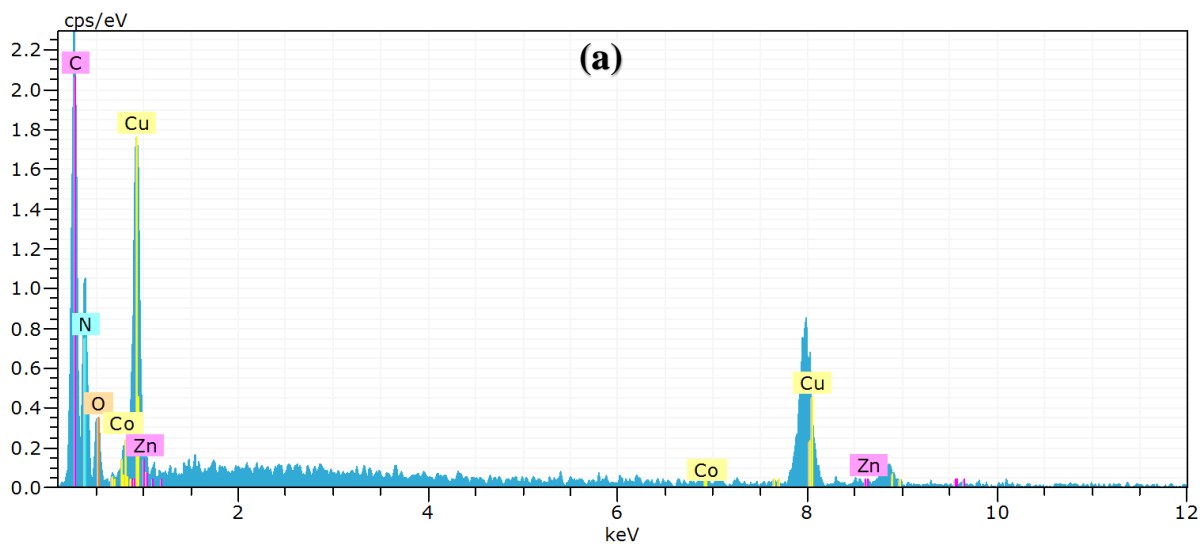
196

197
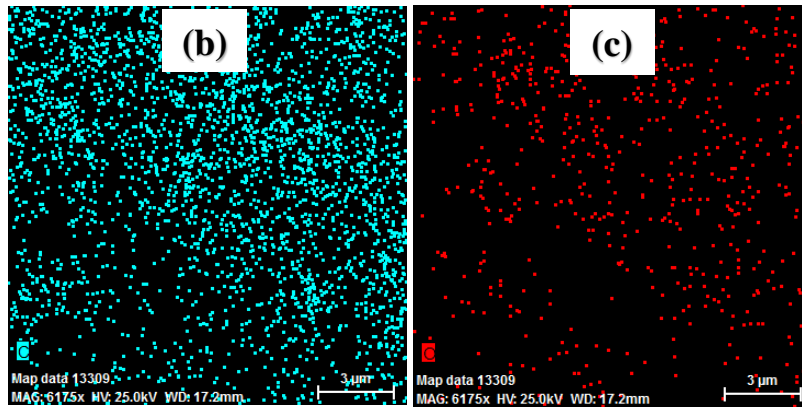
198

199

200

201 **Figure 7.** (a) EDS analysis and the corresponding elemental mapping analysis of (b) carbon (cyan),

202 (c) oxygen (red), (d) nitrogen (purple), (e) zinc (blue), (f) copper (green), (g) cobalt (yellow) and

203 (h) the overlapping of O, N, C, Zn, Co and Cu elements in $ZnCo_2O_4/g-C_3N_4/Cu$.

204

205 **The role of impressive parameters on the solar light-mediated photocatalytic degradation of**
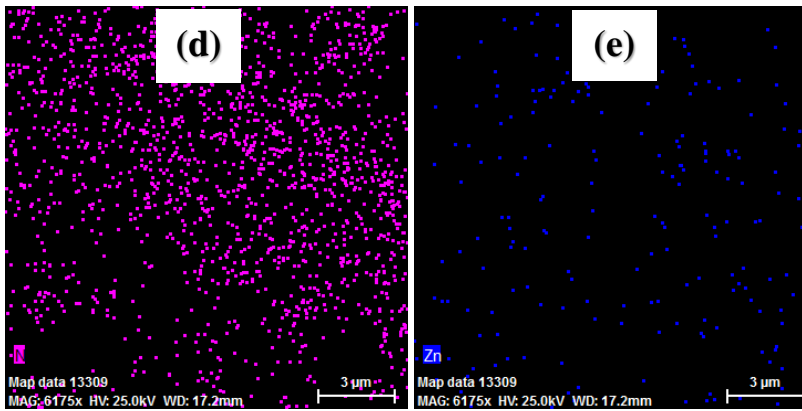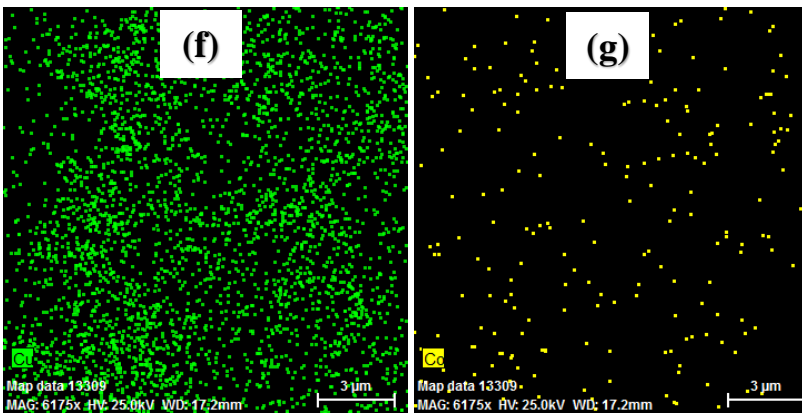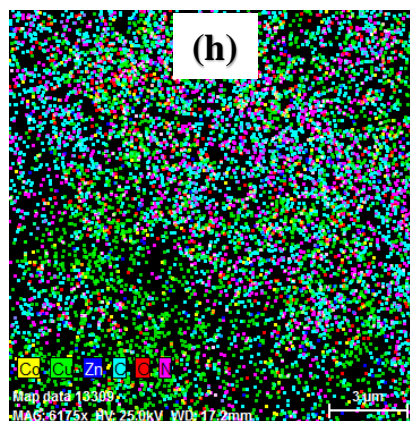
206 **MNZ using $ZnCo_2O_4/g-C_3N_4/Cu$**

207 MNZ (Figure 8), as an important derivative of nitroimidazole antibiotic, is one of the most widely

208 used antibiotics in the world.[41] MNZ that has anti-inflammatory and antibacterial properties is

209 commonly applied in the treatment of infectious diseases caused by anaerobic bacteria and

210 protozoa such as *Giardia lamblia* and *Trichomonas vaginalis.*[42,43] It is also utilized as an additive

211 in poultry, cattle, and fish feed for parasites elimination.[44] Low biodegradability and high water

212 solubility of MNZ results in serious aquatic environmental damages.[45,46] To the best of our

213 knowledge, applying the natural sunlight as an irradiation source for the photocatalytic degradation

214 of MNZ is limited to a few approaches.[47-49] The majority of these approaches suffer from one or

215 more of the following shortcomings comprising the low degradation efficiency, the use of large

216 quantities of the photocatalyst, photocatalyst loss during the recycling, long reaction times,

217 needing the pH adjustment prior to the process, and the utilization of expensive/complex

218 photocatalysts. Therefore, the development of a more sustainable, proficient and convenient

219 method for the MNZ degradation is a mandatory issue.

220
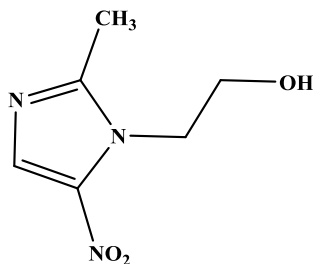
221 **Figure 8.** Chemical structure of MNZ molecule.

222

223 **The influence of pH**

224 The pH value plays an imperative role in the photocatalytic degradation process of pollutants,

225 especially the pharmaceutical compounds. In the next experiment, the influence of pH variation

226 on photocatalytic degradation efficacy of MNZ was studied as a function of the radiation time.

227 The relating tests were set at pH range from 3 to 11 as displayed in Figure 9. As it is evident in the

228 diagram, a maximum value (98%) of the MNZ degradation efficacy was acquired at neutral pH,

229 whilst the degradation rate was dramatically dropped in acidic and alkaline pH values. This

230 observation might be ascribed to the unsuitable interactions of the MNZ molecules and

231 $ZnCo_2O_4/g-C_3N_4/Cu$ in acidic and alkaline solutions.[50] The high degradation reactivity of

232 $ZnCo_2O_4/g-C_3N_4/Cu$ at neutral pH is considered a privilege, since the pH adjustment step is

233 eliminated prior the photocatalytic treatment.

234

235
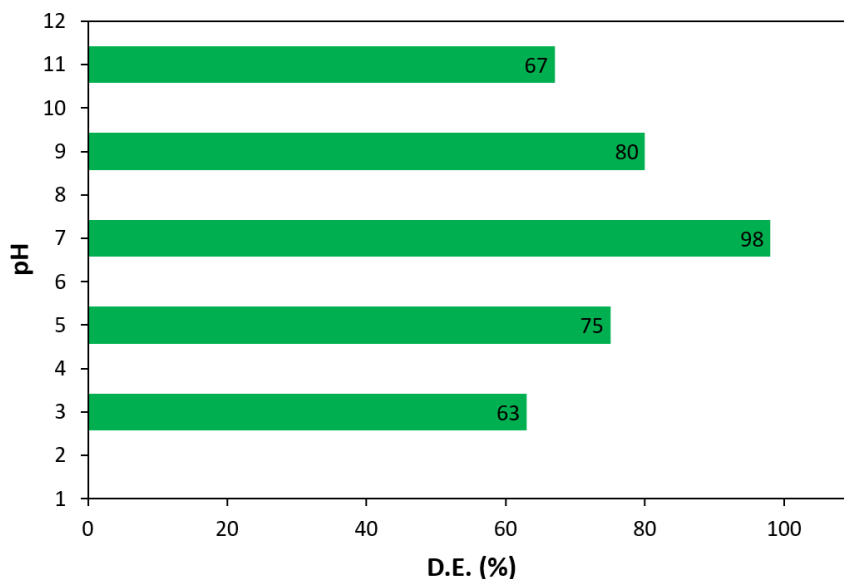
Figure 9. The influence of different pH values on MNZ degradation efficacy (MNZ concentration = 20 mg L^{-1}, photocatalyst dosage = 0.02 g L^{-1}, and reaction time = 30 min).

The effect of ZnCo$_2$O$_4$/g-C$_3$N$_4$/Cu amount and contact time

The amount of the applied photocatalyst has a fundamental effect in the photocatalytic procedures.[51] Accordingly, the effect of ZnCo$_2$O$_4$/g-C$_3$N$_4$/Cu amount was studied as a variable factor (0.005–0.05 g L^{-1}) towards the MNZ degradation under solar light irradiation. The experiments were accomplished using a solution of MNZ with a determined concentration of 20 mg L^{-1} and at pH 7. The obtained results in Figure 10 shown that the efficiency of the MNZ degradation process initially enhanced with the increase of the photocatalyst amount, and then began to decrease in such a way that by using 0.005, 0.02, and 0.05 g L^{-1} of the photocatalyst, the degradation efficiency (in 30 min) obtained to be 80%, 98%, and 41%, respectively. The reason for the rise in the degradation percentage with the increase of photocatalyst amount from 0.005 to 0.02 g L^{-1} was that the number of active catalytic sites increases in parallel with the enhancement of the photocatalyst amount, which consequently raise the feasibility of contact between the photocatalyst and the MNZ. On the other hand, the reduction in the MNZ degradation efficiency with further enhancing the catalyst amount (from 0.02 to 0.05 g L^{-1}) could be related to the reduced light scattering caused by the solution turbidity.[52]

The effect of the contact time was also probed. As it can be seen in Figure 10, the degradation percent strongly increased up to 30 min, whereas with further time passing, the MNZ degradation process made no more progress. This is due to the reason that there are not adequate active hydroxyl radical species in the solution. Therefore, the optimum amount of the photocatalyst was determined to be 0.02 g L^{-1} within the optimized time of 30 min.

259
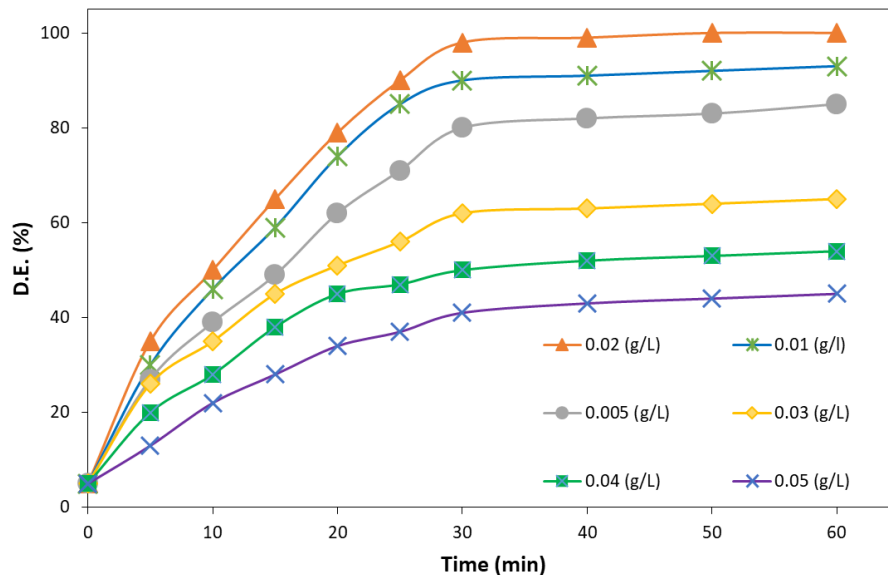
260

261

262   **Figure 10.** The effect of photocatalyst loading on MNZ degradation efficacy (MNZ

263   concentration = 20 mg L^{-1}, and pH = 7).

264

265

The effect of MNZ concentration

267   The primary concentration of the target contaminant essentially affects the photocatalytic

268   degradation efficiency. To evaluate the effect of MNZ concentration on the photocatalytic

269   degradation performance of ZnCo$_2$O$_4$/g-C$_3$N$_4$/Cu, a broad range of MNZ concentrations (10 to 30

270   mg L^{-1}) was tested by keeping other experimental conditions at the obtained optimum values. The

271   results are depicted in Figure 11. As observed, high photocatalytic degradation performance was

272   attained at lower initial MNZ concentrations (10–20 mg L^{-1}) whereas the degradation percentage

273   drastically decreased as the MNZ concentration increased. This result is due to the fact that at

274   lower concentrations of MNZ, the possibility of the reaction between reactive species and MNZ

19

275 molecules enhances. Moreover, at higher concentrations of MNZ, the excess of the amount of the

276 contaminant molecules were amassed on the surface of the catalyst, which hinders the suitable

277 penetration of the sunlight irradiation to the active sites of the photocatalyst.[50] Based on the results

278 obtained, the maximum degradation rate of MNZ was obtained to be 20 mg L^{-1}.
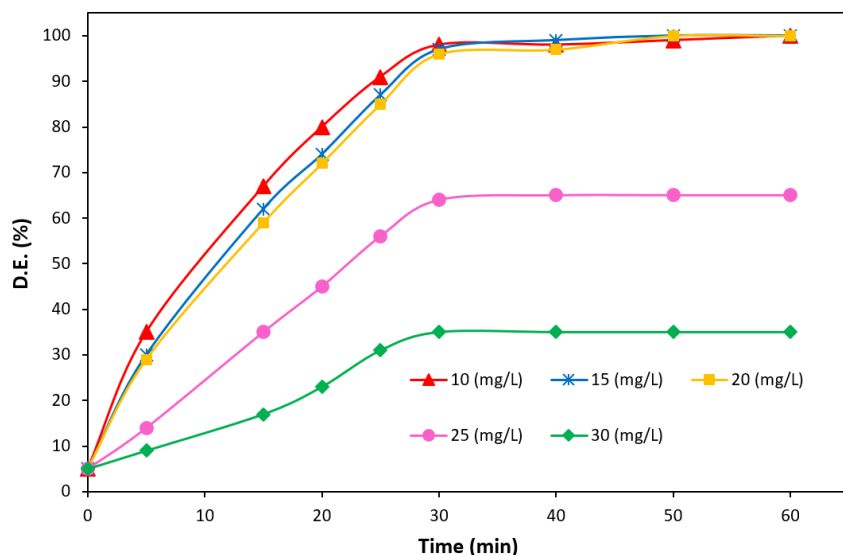
279

280 **Figure 11.** The effect of MNZ concentration on its degradation efficacy (photocatalyst dose =

281 0.02 g L^{-1}, and pH = 7).

282 To further clarify the photocatalytic capability of the $ZnCo_2O_4/g-C_3N_4/Cu$, control experiments

283 were carried out under the optimal conditions. For this purpose, the photolysis experiment of MNZ

284 (*i. e.* with no photocatalyst) under the sun light irradiation, and the possibility of MNZ adsorption

285 on the photocatalyst surface at dark conditions were investigated. Figure 12 reveals that the

286 photolysis test was not accompanied by any progress in the process. Moreover, the obtained results

287 from the adsorption test showed that the capability of the photocatalyst for the adsorption of MNZ

288 under the dark condition is less than 5%.

289 In the following, the ability of $g-C_3N_4$ and $ZnCo_2O_4/g-C_3N_4$ were studied separately for the

290 photocatalytic degradation of MNZ under the optimal conditions and the degradation efficiencies

291   were calculated to be 43% and 65 %, respectively. Nevertheless, it is apparent that by using

292   ZnCo$_2$O$_4$/g-C$_3$N$_4$/Cu under the optimal conditions, the best MNZ degradation efficiency was

293   obtained within 30 minutes. It is supposed that the synergistic optical effect between g-C$_3$N$_4$,

294   ZnCo$_2$O$_4$ and Cu is responsible for the enhancement in the degradation efficiency, through the

295   increase of the production of charge carriers and effectually decrease the recombination speed of

296   the electron-hole pairs (Figure 12).
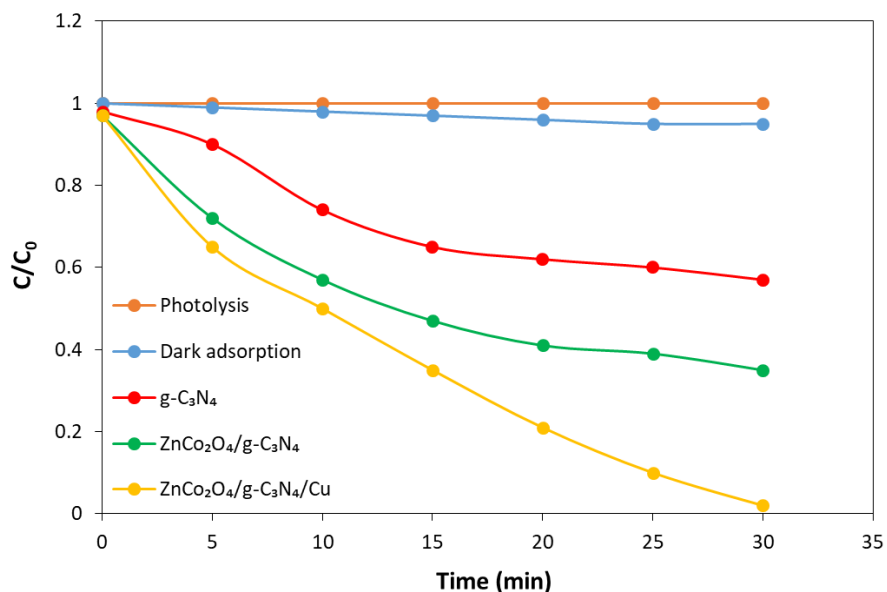
297

298   **Figure 12.** Photocatalytic degradation of MNZ under the solar light irradiation under optimal

299   conditions.

300

301   **Kinetic study**

302   One of the fundamental aspects in the catalytic wastewater treatments is the evaluation of the

303   process rate kinetics. The Langmuir–Hinshelwood (L-H) kinetic model has been widely used for

304   the investigation of the photocatalytic degradation rates of several pollutants, particularly the

305   pharmaceutical compounds.[53,54] In this context, an effectual photocatalytic degradation approach

306   conforms to the pseudo first-order kinetics with respect to the L-H model:

307     $\ln(\frac{C_0}{C_t}) = -kt$

308   where, C_0 is the initial concentration of the pollutant (mg L^{-1}), and C_t is the remaining

309   concentration of the pollutant after the given time t (mg L^{-1}), t represents the specific reaction time

310   (min) and k is the pseudo-first-order rate constant, which can be determined from the slope of the

311   straight line, when plotting the graph of ln (C_0/C_t) *vs*. contact time (t).

312   To assess the kinetics of the photocatalytic degradation of MNZ in the presence of the ZnCo$_2$O$_4$/g-

313   C$_3$N$_4$/Cu, some typical experiments were implemented under the optimal conditions (pH = 7, and

314   catalyst dosage = 0.02 g L^{-1}) for different concentrations of MNZ within the range of 5-30 min. As

315   it is clear in the degradation reaction curves (Figure 13), there is a linear relationship between ln

316   (C_0/C_t) and the irradiation times. According to these findings, it is perceived that the photocatalytic

317   degradation process of MNZ in the presence of ZnCo$_2$O$_4$/g-C$_3$N$_4$/Cu followed a pseudo-first-order

318   kinetics.

319   Furthermore, the calculated values for the coefficient of determination (R^2) were obtained close to

320   1 for all MNZ concentrations, which is another evidence to confirm the appropriateness of the

321   degradation process (Table 1). It is worth to note that, as the concentration of MNZ increased, the

322   reaction rate constant decreased. This result can be justified on the basis of the hypothesis that at

323   higher MNZ concentrations, the enhancement of the intermediate products might take place, which

324   leads to diminish the potent hydroxyl radical specie in the solution and consequently the

325   degradation rate constants.[51]
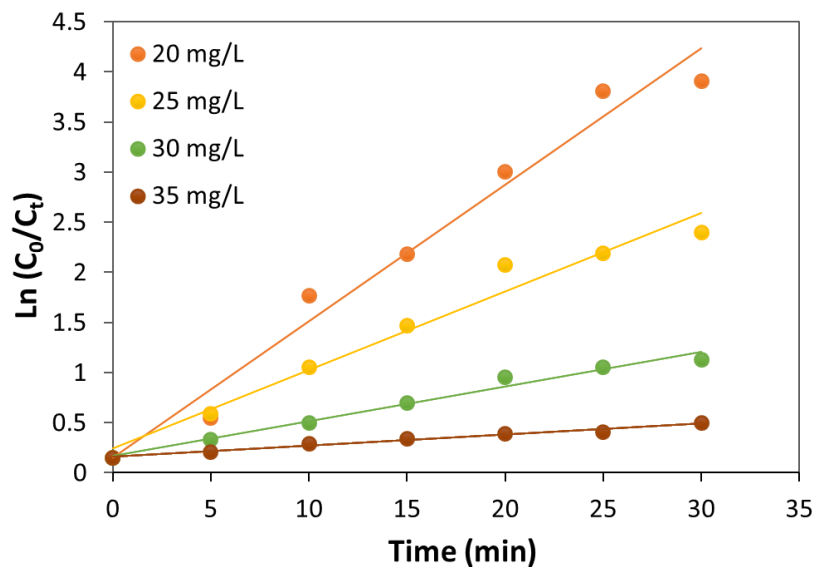
Figure 13. Plots of ln (C_0/C_t) *vs.* irradiation time for photocatalytic degradation of MNZ at different concentrations (pH = 7 and catalyst dosage = 0.02 g L^{-1}).

Table 1. Kinetic parameters for MNZ photocatalytic degradation reactions at different concentrations.

Entry	MNZ concentration (mg L^{-1})	Equation	K (min^{-1})	R^2
1	20	y = 0.1359x + 0.1568	135.9×10^{-3}	0.9749
2	25	y = 0.0784x + 0.2418	78.4×10^{-3}	0.9730
3	30	y = 0.0345x + 0.1696	34.5×10^{-3}	0.9824
4	35	y = 0.0111x + 0.1611	11.1×10^{-3}	0.9824

Reusability of ZnCo₂O₄/g-C₃N₄/Cu in the photocatalytic degradation process of MNZ

Surveying the recyclability of the photocatalysts, as well as their stability, is one of the important parameters in the practical photocatalytic applications. Accordingly, to investigate the potential of recycling of ZnCo₂O₄/g-C₃N₄/Cu, the photocatalytic degradation of MNZ was performed in eight consecutive runs under optimum conditions. When each reaction cycle finished, the photocatalyst

23

337   was isolated from aqueous solution by simple centrifugation. Then, the separated photocatalyst

338   was washed several times with distilled H_2O. It was subsequently dried in a vacuum oven at 80 °C

339   for 2 h to be ready for use in the next photocatalytic reaction run. The results of these experimental

340   series are depicted in Figure 14. As it is apparent, there was no obvious reduction in the

341   photocatalytic activity of $ZnCo_2O_4$/g-C_3N_4/Cu even after eight recycling times. The small drop in

342   the MNZ photocatalytic degradation percentage can be allocated to the slight photocatalyst loss

343   during the recycling steps.

344   Comparing the FT-IR spectrum, FESEM and TEM images of the eight times reused catalyst

345   (Figure 15 and 16) with those of the fresh one (Figure 1b and 6), evidently showed the preservation

346   of the morphology and structure of the photocatalyst after the sequential runs.

347
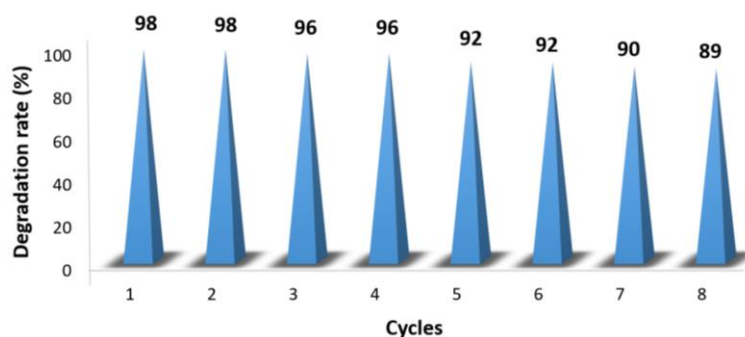
348

349   **Figure 14.** Cycling runs for the photocatalytic degradation of MNZ over the $ZnCo_2O_4$/g-

350   C_3N_4/Cu nanocomposite.

351
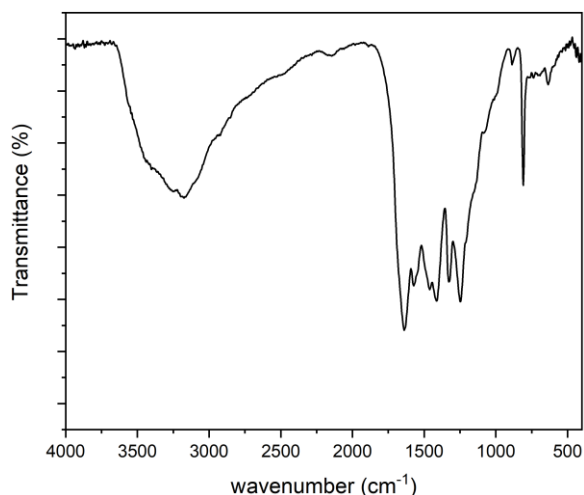
Figure 15. FT-IR spectrum of ZnCo$_2$O$_4$/g-C$_3$N$_4$/Cu after eight times reused.

353
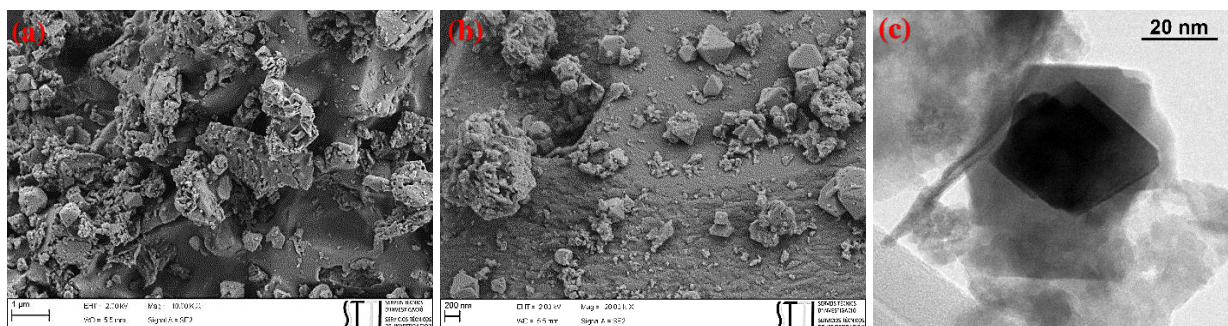
Figure 16. (a, b) FESEM of ZnCo$_2$O$_4$/g-C$_3$N$_4$/Cu and (c) TEM of ZnCo$_2$O$_4$/g-C$_3$N$_4$/Cu after

355   eight times reused.

356

357 **Comparative study**

358 Literature review was carried out to compare the advantages of presented procedure over the

359 almost all similar previous reported methods towards the MNZ photocatalytic degradation (Table

360 2). As it is observable from the obtained results, the represented photocatalytic methodology for

361 MNZ degradation in this study is preferred to the reported ones. The supreme photocatalytic ability

362 of ZnCo$_2$O$_4$/g-C$_3$N$_4$/Cu could be correspond to the synergistic optical effects between ZnCo$_2$O$_4$,

363 g-C3N4, and Cu, which increased the production of charge carriers and successfully reduced the

364 recombination rate of the electron-hole pairs.

365

366 **Table 2.** Comparison of the photocatalytic efficiency of $ZnCo_2O_4/g-C_3N_4/Cu$ with some of the reported photocatalytic

367 systems for MNZ degradation under visible/sunlight irradiation. SARA DID YOU TEST THE PHOTO-

368 DEGRADATION IN THE ABSENCE OF CATALYST?

Entry	Photocatalyst	Light source	Catalyst dosage (g L^{-1})	MNZ concentration (mg L^{-1})	pH	Time (min)	Degradation efficiency (%)	Ref.
1	FeNi$_3$/chitosan/BiOI	Xenon lamp (420 nm filter, 500 W)	0.04	20	7	200	100	50
2	D-g-C$_3$N$_4$-Bi$_5$O$_7$I	Halogen lamp (300 W), λ>420 nm	0.8	15	10	6 h	89	55
3	Fe/Si codoped TiO$_2$ (H$_2$O$_2$: 10 mM)	Xenon lamp (220 W)	0.3	6	7	50	93	56
4	Phosphorus-doped g-C$_3$N$_4$ /Co$_3$O$_4$ QDs[a]	Xenon lamp (250 W), λ>420 nm	1	10	-[b]	180	80	57
5	ZnS-NiS/zeolite	Hg-lamp (35 W)	3	4	2	150	93.98	58
6	Ag$_2$S/BiVO$_4$@a-Al$_2$O$_3$	LED strips (6 W, λ = 420	1	10	3	90	92.2	59
7	Fe$_3$O$_4$/rGO/TiO$_2$	Xe lamp (150W)	0.75	20	5	120	96	60

26

8	SnO$_2$/NiO-NC[c]	Sunlight	1.2	2	3	180	-[b]	47
9	Ag-h-TiO$_2$[d]	HPMV[e] lamp (125 W)	0.5	15	-[b]	210	96.55	61
10	MoO$_3$/MgAl-LDH-C[f]	Sunlight	1.5	10	7	60	80	48
11	Urea/TiO$_2$/ZnFe$_2$O$_4$/Clinoptiloite	Visible light LED 400	2	100	5	120	95.6	62
12	CDS QDs[a]-TiO$_2$	Visible light Xe lamp 300W	0.04	5	-[b]	60	90.9	63
13	TiO$_2$	Sunlight	1.2	5	12	300	90	49
14	BiVO$_4$/FeVO$_4$	Xe lamp (500 W)	4	10	-[b]	90	91	64
15	CdS/g-C$_3$N$_4$	Xe lamp (500 W)/ λ≤400 nm	0.1	5	-[b]	5 h	98	65
16	Bi$_4$VO$_8$Cl	Xe lamp (300 W)/ λ>420 nm	1	10	-[b]	10 h	100	66
17	ZnCo$_2$O$_4$/g-C$_3$N$_4$/Cu	Sunlight	0.02	20	7	30	98	Present study

[a] QDs = quantum dots; [b] This data was not mentioned in the article; [c] NC = clinoptilolite NPs; [d] silver doped hollow TiO$_2$ NPs; [e] High pressure mercury vapor; [f] The letter C refers to calcined samples and LDH = layered double hydroxides.

In a further development, the radical/hole scavenger trapping tests were accomplished for elucidating the major oxidative species in MNZ photocatalytic degradation method. For this purpose, photocatalytic degradation of MNZ was performed under optimal conditions in the

375   presence of isopropanol (IPA), benzoquinone (BQ) and triethylamine (TEA) in turn as the

376   hydroxyl radical, superoxide radical, and hole scavengers (Figure 17). As shown in Figure 17,

377   without using any scavenger in the photocatalytic process, the efficiency of the MNZ degradation

378   in the presence of $ZnCo_2O_4$/g-C_3N_4/Cu was about 98% within 30 min. By the addition of BQ (1

379   mM) or TEA (1 mM) to the reaction medium, the progress of the MNZ degradation was

380   dramatically decreased. However, when IPA (1 mM) was added to the reaction solution, a

381   moderate effect on the MNZ photocatalytic degradation efficiency was observed. Accordingly, it

382   can be concluded that the major role in the development of the present photocatalytic system is

383   concerned with superoxide radical and hole species.

384
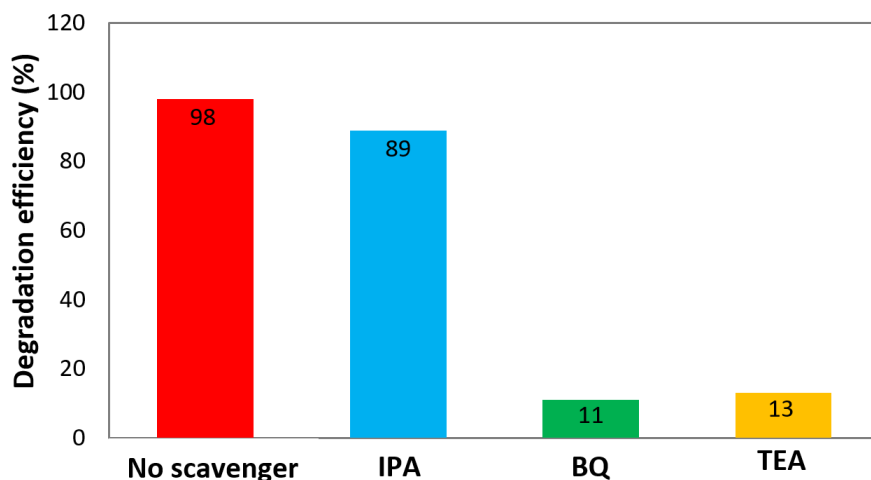
Figure 17. The radical/hole scavengers effects on MNZ photocatalytic degradation efficiency in

386   the presence of $ZnCo_2O_4$/g-C_3N_4/Cu, within the optimized conditions.

387

388   Having these results in hand, a possible photocatalytic mechanism was presented for the MNZ

389   photocatalytic degradation by using $ZnCo_2O_4$/g-C_3N_4/Cu under the solar light radiation (Figure

390   18). The schematic demonstrated in Figure 18 displays the pathway of the electron-hole separation

391   and charge transfer over the $ZnCo_2O_4$/g-C_3N_4/Cu interfaces. Under the sunlight irradiation,

28

392   electrons and holes can be simply produced through the stimulation of $ZnCo_2O_4$ and g-C_3N_4.

393   Thereupon, the photogenerated electrons accumulated on the conduction bond (CB) of $ZnCo_2O_4$,

394   can be quickly transferred into the CB of g-C_3N_4 and simultaneously the existing electrons on the

395   CB of g-C_3N_4 injected to Cu. Meanwhile, the photogenerated holes in the valence bond (VB) of g-

396   C_3N_4 can be easily immigrated into VB of $ZnCo_2O_4$. These appropriate transformations of the

397   charge carries along the heterojunction interfaces of the $ZnCo_2O_4$/g-C_3N_4/Cu resulted to the

398   efficient separation of photogenerated electron and hole pairs, which could suitably prolong the

399   lifetime of the corresponding excited electrons and holes. The superoxide radicals, which have

400   strong oxidative features for the photocatalytic degradation of MNZ, would be further generated

401   by the electrons injected into Cu. On the other hand, the holes transferred to the VB of $ZnCo_2O_4$

402   can directly participate in the MNZ degradation.

403

404

29
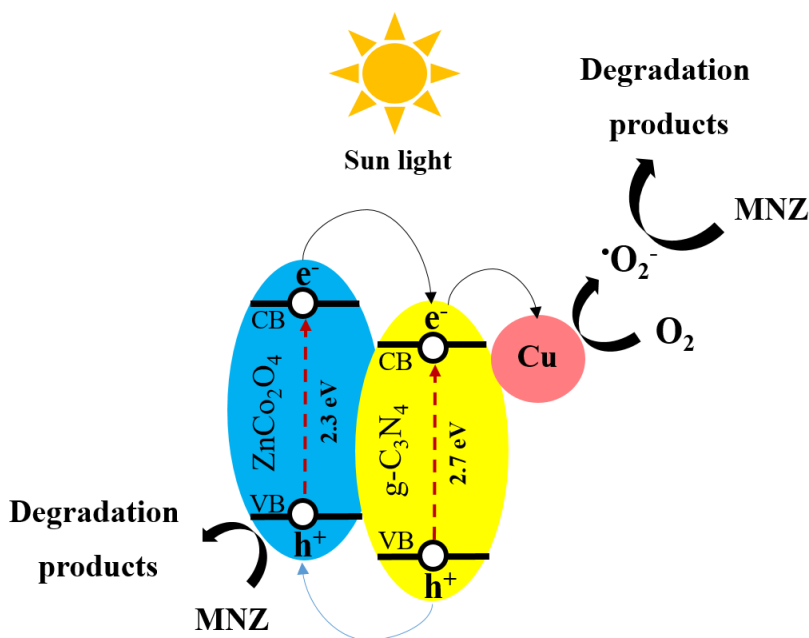
Figure 18. Proposed photocatalytic mechanism for the sunlight induced photocatalytic degradation of MNZ in the presence of $ZnCo_2O_4/g\text{-}C_3N_4/Cu$.

EXPERIMENTAL SECTION

Chemicals and reagents

All solvents and chemicals were purchased from Merck chemical company. MNZ tablets (400 mg) were provided by Jaber Ebne Hayyan pharmaceutic company. Sodium hydroxide and hydrochloric acid consumed for pH adjustment. Deionized water was utilized during the entire study.

Instrumentation

The progress of the degradation process was monitored by UV-vis spectrophotometer (Shimadzu, 2501-PC, Kyoto, Japan). Transmission electron microscopy (TEM) is carried out using the TEM microscope JEOL JEM-1400 Plus. SEM microscopy was performed in a Hitachi model S3000N. FT-IR spectra are recorded on a Shimadzu Fourier Transform Infrared Spectrophotometer (FT-IR-8300). X-ray diffraction (XRD) is carried out on an Xpert Pro Panalytical diffractometer (PW1730, PHILIPS company) with Cu Kα radiation (λ = 1.540 Å). X-ray photoelectron spectroscopy (XPS) analyses are done using a VG-Microtech Multilab 3000 spectrometer, equipped with an Al anode. The deconvolution of the spectra is performed through Gaussian Lorentzian curves. UV-vis diffuse reflectance spectroscopy (DRS) is conducted using a Shimadzu spectrophotometer (UV-2550 model). Energy-dispersive X-ray spectroscopy (EDS) and elemental mapping are accomplished by a TESCAN MIRA3. A glass-combination of electrode equipped with digital pH-meter (HANNA instruments HI 2211 pH/ORP Meter) is utilized for the pH control.

Synthesis of the photocatalyst

Synthesis of g-C₃N₄ NSs

According to a modified previously described procedure, the consecutive polymerization and liquid exfoliation procedures were performed for preparing g-C_3N_4 NSs.[67] In a typical experiment, 5 g of melamine powder was poured to a covered crucible and calcined at 550 °C (heating rate = 5 °C min^{-1}) for 3 h. The resulting agglomerated yellow solid was cooled down to ambient temperature. Then it was milled thoroughly to obtain the uniform bulk g-C_3N_4 powder. Afterward, 0.1 g of the acquired bulk g-C_3N_4 powder was dissolved in 100 mL of deionized water and sonicated for 6 h. Next, the obtained suspension was centrifuged (5000 rpm) to remove the remaining un-exfoliated g-C_3N_4. Finally, the g-C_3N_4 NSs were attained after vacuum drying.

Synthesis of ZnCo₂O₄/g-C₃N₄

$Zn(NO_3)_2 \cdot 6H_2O$ (0.14 mmol) and $Co(NO_3)_2 \cdot 6H_2O$ (0.28 mmol) were dispersed in 80 mL distilled water for 30 min. Then, a 2 M solution of NaOH was added dropwise into the mixture at ambient temperature to adjust the solution pH to 10. The obtained suspension was vigorously stirred at ambient temperature for 30 min. The previously synthesized g-C_3N_4 NSs (0.5 g) were added to this solution. The obtained suspension underwent the reflux temperature for 1 h. Thereafter, the resulting solution was centrifuged, washed repeatedly with deionized water and vacuum-dried. Finally, the resulting powder was heated at 350 °C for 2 h to afford the desired $ZnCo_2O_4$/g-C_3N_4.

Synthesis of ZnCo₂O₄/g-C₃N₄/Cu

After being dispersed in EtOH (30 mL) for 30 min, the as-synthesized $ZnCo_2O_4$/g-C_3N_4 (1 g) was gradually treated with a solution of $Cu(OAc)_2$ (2 mmol) in 15 mL EtOH and continuous stirred for 1 h. To the resulting suspension, an aqueous solution of $NaBH_4$ (30 mL, 0.1 M) was poured dropwise, under vigorous stirring. After 4 h, the resulting $ZnCo_2O_4$/g-C_3N_4/Cu was separated by

450 centrifugation, washed repeatedly with distilled water and ethanol (3 × 15 mL) and vacuum-dried

451 at 60 °C.

452 **Degradation of MNZ by Solar light in the presence of ZnCo$_2$O$_4$/g-C$_3$N$_4$/Cu as a photocatalyst**

453 MNZ degradation experiments were performed at room temperature in a batch reactor with a

454 capacity of 500 ml. In all experiments, the solutions were exposed to the sunlight from 11 a.m. to

455 3 p.m. and continuous magnetic stirring (350 rpm) was performed to ensure the homogeneity of

456 the suspension. The constant supply of oxygen was assured by means of an air pump. The

457 degradation ability of ZnCo$_2$O$_4$/g-C$_3$N$_4$/Cu was tested by the evaluation of different factors

458 including pH (3, 5, 7, 9, and 11), contact time (up to 60 min), catalyst amount (0.005–0.05 g L^{-1})

459 and concentration of MNZ (10–30 mg L^{-1}). Prior to the illumination in each run, the mixture was

460 stirred in dark conditions (30 min) to guarantee that the adsorption−desorption equilibrium was

461 reached. Then, at specific time intervals (5 min) of the reaction, a 2 mL portion of the suspension

462 was sampled out and centrifuged to separate the photocatalyst from the solution. Finally, to

463 determine the residual concentration of MNZ in the solution bath, the filtrate was analyzed by UV-

464 vis spectrophotometer at 320 nm. The efficiency of the MNZ degradation process was measured

465 using the following equation.

466

467 $Degradation\ efficiency\ (\%) \ = \dfrac{C_0 - C_t}{C_0} \times 100$

468

469 where, C_o and C_t are the concentrations of MNZ at initial and at a particular time of t, respectively.

470

471

CONCLUSIONS

In this study, $ZnCo_2O_4$/g-C_3N_4/Cu nanocomposite was synthesized and sufficiently characterized. The ability of the synthesized $ZnCo_2O_4$/g-C_3N_4/Cu was satisfactorily evaluated towards the sunlight-driven photocatalytic degradation of aqueous solution of MNZ. Under the optimal conditions (photocatalyst dosage = 0.02 g L^{-1}, MNZ concentration = 20 mg L^{-1}, pH = 7, and irradiation time = 30 min), the MNZ photocatalytic degradation efficiency is attained to be 98%. Fascinatingly, the superlative photocatalytic performance of the photocatalyst might be related to the synergistic optical effects of $ZnCo_2O_4$, g-C_3N_4, and Cu, which can not only raise the production of charge carriers but also overcome the rapid rate of the photo-induced electron/hole pairs recombination. With respect to the L-H model, the attained experimental amounts in this work, are clearly consistent with the pseudo first-order kinetics. This approach offers several advantages such as using natural sunlight source, neutrality of the reaction medium, short reaction time, applying very low amount of the photocatalyst, high efficiency of the degradation process, utilizing air as the oxidant, low operational cost and ease of the catalyst recycling for at least eight times with only 9% reduction in the degradation efficiency. SARA I SUGGEST YOU TO PUT ATTENTION AND ENPHASIS IN THE ADVANTAGES OF YOUR METHOD, AS LOWER CATALYST LOADING, CONCENTRATION OF THE SAMPLE, TIME PH (TABLE 2).

495

REFERENCES

(1) Davies, J.; Davies, D. Origins and evolution of antibiotic resistance. *Microbiol. Mol. Biol. Rev.* **2010**, *74* (3), 417–433.

(2) Wang, M.; Zhang, L.; Zhang, G.; Pang, T.; Zhang, X.; Cai, D.; Wu, Z. In situ degradation of antibiotic residues in medical intravenous infusion bottles using high energy electron beam irradiation. *Sci. Rep.* **2017**, *7* (1), 1–8.

(3) Blackbeard, J.; Lloyd, J.; Magyar, M.; Mieog, J.; Linden, K. G.; Lester, Y. Demonstrating organic contaminant removal in an ozone-based water reuse process at full scale. *Environ. Sci. Water Res. Technol.* **2016**, *2* (1), 213–222.

(4) Huang, A.; Yan, M.; Lin, J.; Xu, L.; Gong, H.; Gong, H. A review of processes for removing antibiotics from breeding wastewater. *Int. J. Environ. Res. Public Health* **2021**, *18* (9), 4909.

(5) Saitoh, T.; Shibata, K.; Fujimori, K.; Ohtani, Y. Rapid removal of tetracycline antibiotics from water by coagulation-flotation of sodium dodecyl sulfate and poly (allylamine hydrochloride) in the presence of Aluminum(III) ions. *Sep. Purif. Technol.* **2017**, *187*, 76–83.

(6) Li, Y.; Liu, L.; Yang, F. Destruction of tetracycline hydrochloride antibiotics by FeOOH/TiO$_2$ granular activated carbon as expanded cathode in low-cost MBR/MFC coupled system. *J. Membr. Sci.* **2017**, *525*, 202–209.

(7) Derakhshan, Z.; Mokhtari, M.; Babaei, F.; Malek Ahmadi, R.; Ehrampoush, M. H.; Faramarzian, M. Removal methods of antibiotic compounds from aqueous environments– a review. *J. Environ. Health Sustain. Dev.* **2016**, *1* (1), 43–62.

518 (8) Ji, L.; Chen, W.; Duan, L.; Zhu, D. Mechanisms for strong adsorption of tetracycline to

519   carbon nanotubes: a comparative study using activated carbon and graphite as adsorbents.

520   *Environ. Sci. Technol.* **2009**, *43* (7), 2322–2327.

521 (9) Zhou, S.; Shao, Y.; Gao, N.; Zhu, S.; Ma, Y.; Deng, J. Chlorination and chloramination of

522   tetracycline antibiotics: disinfection by-products formation and influential factors.

523   *Ecotoxicol. Environ. Saf.* **2014**, *107*, 30–35.

524 (10) Slipko, K.; Reif, D.; Wögerbauer, M.; Hufnagl, P.; Krampe, J.; Kreuzinger, N. Removal of

525   extracellular free DNA and antibiotic resistance genes from water and wastewater by

526   membranes ranging from microfiltration to reverse osmosis. *Water Res.* **2019**, *164*,

527   114916.

528 (11) Elmolla, E. S.; Chaudhuri, M. Comparison of different advanced oxidation processes for

529   treatment of antibiotic aqueous solution. *Desalination* **2010**, *256* (1-3), 43–47.

530 (12) Hachem, C.; Bocquillon, F.; Zahraa, O.; Bouchy, M. Decolourization of textile industry

531   wastewater by the photocatalytic degradation process. *Dyes Pigm.* **2001**, *49* (2), 117–125.

532 (13) Qi, X. H.; Zhuang, Y. Y.; Yuan, Y. C.; Gu, W. X. Decomposition of aniline in supercritical

533   water. *J. Hazard. Mater.* **2002**, *90* (1), 51–62.

534 (14) Chen, C.; Ma, W.; Zhao, J. Semiconductor-mediated photodegradation of pollutants under

535   visible-light irradiation. *Chem. Soc. Rev.* **2010**, *39* (11), 4206–4219.

536 (15) Safari, G. H.; Hoseini, M.; Seyedsalehi, M.; Kamani, H.; Jaafari, J; Mahvi, A. H.

537   Photocatalytic degradation of tetracycline using nanosized titanium dioxide in aqueous

538   solution. *Int. J. Environ. Sci. Technol.* **2015**, *12* (2), 603–616.

539 (16) Yang, M. Q.; Shen, L.; Lu, Y.; Chee, S. W.; Lu, X.; Chi, X.; Chen, Z.; Xu, Q. H.;

540   Mirsaidov, U.; Ho, G. W. Disorder engineering in monolayer nanosheets enabling

541   photothermic catalysis for full solar spectrum (250–2500 nm) harvesting. *Angew. Chem.*

542   *Int. Ed.* **2019**, *58* (10), 3077–3081.

543 (17) Lim, P. F.; Leong, K. H.; Sim, L. C.; Oh, W. D.; Chin, Y. H.; Saravanan, P.; Dai, C.

544   Mechanism insight of dual synergistic effects of plasmonic Pd-$SrTiO_3$ for enhanced solar

545   energy photocatalysis. *Appl. Phys. A* **2020**, *126* (7), 1–10.

546 (18) Sharma, M.; Jain, T.; Singh, S.; Pandey, O. P. Photocatalytic degradation of organic dyes

547   under UV–Visible light using capped ZnS nanoparticles. *Sol. Energy* **2012**, *86* (1), 626–

548   633.

549 (19) Ong, W. J.; Tan, L. L.; Ng, Y. H.; Yong, S. T.; Chai, S. P. Graphitic carbon nitride (g-

550   C_3N_4)-based photocatalysts for artificial photosynthesis and environmental remediation:

551   are we a step closer to achieving sustainability? *Chem. Rev*. **2016**, *116* (12), 7159−7329.

552 (20) Wang, Y.; Wang, X. C.; Antonietti, M. Polymeric graphitic carbon nitride as a

553   heterogeneous organocatalyst: from photochemistry to multipurpose catalysis to

554   sustainable chemistry. *Angew. Chem., Int. Ed.* **2012**, *51* (1), 68−89.

555 (21) Cao, S. W.; Low, J. X.; Yu, J. G.; Jaroniec, M. Polymeric photocatalysts based on graphitic

556   carbon nitride. *Adv. Mater.* **2015**, *27* (13), 2150−2176.

557 (22) Ran, J. R.; Ma, T. Y.; Gao, G. P.; Du, X. W.; Qiao, S. Z. Porous p-doped graphitic carbon

558   nitride nanosheets for synergistically enhanced visible-light photocatalytic H_2 production.

559   *Energy Environ. Sci.* **2015**, *8* (12), 3708−3717.

560 (23) Li, Z.; Raziq, F.; Liu, C.; Bai, L. Jing, L. Surface-engineering strategies for g-C_3N_4 as

561   efficient visible-light photocatalyst. *Curr. Opin. Green Sustain. Chem*. **2017**, *6*, 57–62.

562 (24) He, Y.; Wang, Y.; Zhang, L.; Teng, B.; Fan, M. High-efficiency conversion of CO_2 to fuel

563   over ZnO/g-C_3N_4 photocatalyst. *Appl. Catal. B: Environ.* **2015**, *168-169*, 1–8.

564 (25) Zhang, W.; Xu, C.; Liu, E.; Fan, J.; Hu, X. Facile strategy to construction Z-scheme

565 $ZnCo_2O_4$/g-C_3N_4 photocatalyst with efficient H_2 evolution activity. *Appl. Surf. Sci.* **2020**,

566 *515*, 146039.

567 (26) Liu, B.; Liu, H.; Liang, M.; Liu, L.; Lv, Z.; Zhou, H.; Guo, H. Controlled synthesis of

568 hollow octahedral $ZnCo_2O_4$ nanocages assembled by untrathin 2D nanosheets for enhanced

569 lithium storage. *Nanoscale* **2017**, *9* (44), 17174–17180.

570 (27) Benhebal, H.; Wolfs, C.; Kadi, S.; Tilkin, R. G.; Allouche, B.; Belabid, R.; Collard, V.;

571 Felten, A.; Louette, P.; Lambert, S. D.; Mahy, J. G. Visible light sensitive SnO_2/$ZnCo_2O_4$

572 material for the photocatalytic removal of organic pollutants in water. *Inorganics*, **2019**, *7*

573 (6), 77.

574 (28) Chen, J.; Zhan, J.; Lu, E.; Wan, Y.; Jin, Z.; Qi, H. Facile template-free fabrication of

575 mesoporous $ZnCo_2O_4$ fibers with enhanced photocatalytic activity under visible-light

576 irradiation. *Mater. Lett*. **2018**, *220*, 66–69.

577 (29) Jung, H.; Pham, T. T.; Shin, E. W. Effect of g-C_3N_4 precursors on the morphological

578 structures of g-C_3N_4/ZnO composite photocatalysts. *J. Alloy. Compd.* **2019**, *788*, 1084–

579 1092.

580 (30) Guan, B.; Guo, D.; Hu, L.; Zhang, G.; Fu, T.; Ren, W.; Li, J.; Li, Q. Facile synthesis of

581 $ZnCo_2O_4$ nanowire cluster arrays on Ni foam for high-performance asymmetric

582 supercapacitors. *J. Mater. Chem. A* **2014**, *2* (38), 16116–16123.

583 (31) Zhang, P. Y.; Song, T.; Wang, T. T.; Zeng, H. P. In-situ synthesis of Cu nanoparticles

584 hybridized with carbon quantum dots as a broad spectrum photocatalyst for improvement

585 of photocatalytic H_2 evolution. *Appl. Catal. B Environ*. **2017**, *206*, 328–335.

586   (32) Huo, J. P.; Zeng, H. P. Copper nanoparticles embedded in the triphenylamine

587   functionalized bithiazole–metal complex as active photocatalysts for visible light-driven

588   hydrogen evolution. *J. Mater. Chem. A* **2015**, *3* (33), 17201–17208.

589   (33) Chen, Y.; Deng, Y.; Pu, Y.; Tang, B.; Su, Y.; Tang, J. One pot preparation of silver

590   nanoparticles decorated TiO_2 mesoporous microspheres with enhanced antibacterial

591   activity. *Mater. Sci. Eng. C* **2016**, *65*, 27–32.

592   (34) Liu, E. Z.; Qi, L. L.; Bian, J. J.; Chen, Y. H.; Hu, X. Y.; Fan, J.; Liu, H. C.; Zhu, C. J.;

593   Wang, Q. P. A facile strategy to fabricate plasmonic Cu modified TiO_2 nano-flower films

594   for photocatalytic reduction of CO_2 to methanol. *Mater. Res. Bull*. **2015**, *68*, 203–209.

595   (35) Zhang, D. Synthesis and characterization of ZnO-doped cupric oxides and evaluation of

596   their photocatalytic performance under visible light. *Transit. Met. Chem*. **2010**, *35* (6),

597   689–694.

598   (36) Jahanshahi, R.; Khazaee, A.; Sobhani, S.; Sansano, J. M. g-C_3N_4/γ-Fe_2O_3/TiO_2/Pd: a new

599   magnetically separable photocatalyst for visible-light-driven fluoride-free Hiyama and

600   Suzuki–Miyaura cross-coupling reactions at room temperature. *New J. Chem.* **2020**, *44*

601   (27), 11513–11526.

602   (37) Jahanshahi, R.; Sobhani, S.; Sansano, J. M. High performance magnetically separable g-

603   C_3N_4/γ-Fe_2O_3/TiO_2 nanocomposite with boosted photocatalytic capability towards the

604   cefixime trihydrate degradation under visible-light. *ChemistrySelect* **2020**, *5* (32), 10114–

605   10127.

606   (38) Bhosale, R.; Jain, S.; Vinod, C. P.; Kumar, S.; Ogale, S. Direct Z-scheme g-C_3N_4/$FeWO_4$

607   nanocomposite for enhanced and selective photocatalytic CO_2 reduction under visible

608   light. *ACS Appl. Mater. Interfaces.* **2019**, *11* (6), 6174–6183.

(39)   Mary, A. J. C.; Bose, A. C. Surfactant assisted $ZnCo_2O_4$ nanomaterial for supercapacitor application. *Appl. Surf. Sci.* **2018**, *449*, 105–112.

(40)   Betancourt-Galindo, R.; Reyes-Rodríguez, P. Y.; Puente-Urbina, B. A.; Ávila-Orta, C. A.; Rodríguez-Fernández, O. S.; Cadenas-Pliego, G.; Lira-Saldivar, R. H.; García-Cerda, L. A. Synthesis of copper nanoparticles by thermal decomposition and their antimicrobial properties. *J. Nanomater.* **2014**, *2014*, 1-5.

(41)   Cheng, W.; Yang, M.; Xie, Y.; Liang, B.; Fang, Z.; Tsang, E. P. Enhancement of mineralization of metronidazole by the electro-Fenton process with a Ce/SnO_2–Sb coated titanium anode. *Chem. Eng. J.* **2013**, *220*, 214–220.

(42)   Fang, Z.; Chen, J.; Qiu, X.; Qiu, X.; Cheng, W.; Zhu, L. Effective removal of antibiotic metronidazole from water by nanoscale zero-valent iron particles. *Desalination* **2011**, *268* 60–67.

(43)   Malakootian, M.; Olama, N.; A. Nasiri. Photocatalytic degradation of metronidazole from aquatic solution by TiO_2-doped Fe^{3+} nano-photocatalyst. *Int. J. Environ. Sci. Technol.* **2019**, *16* (8), 4275–4284.

(44)   Xiao, C.; Ma, K.; Cai, G.; Zhang, X.; Vessally, E. Borophene as an electronic sensor for metronidazole drug: A computational study. *J. Mol. Graph. Model.* **2020**, *96*, 107539.

(45)   Çelik, A.; Aras Ateş, N. The frequency of sister chromatid exchanges in cultured human peripheral blood lymphocyte treated with metronidazole in vitro. *Drug Chem. Toxicol.* **2006**, *29* (1), 85–94.

(46)   Bendesky, A.; Menéndez, D.; Ostrosky-Wegman, P. Is metronidazole carcinogenic?. *Mutat. Res. - Rev. Mutat. Res.* **2002**, *511* (2), 133–144.

(47) Derikvandi, H.; Nezamzadeh-Ejhieh, A. Synergistic effect of p-n heterojunction, supporting and zeolite nanoparticles in enhanced photocatalytic activity of NiO and SnO$_2$. *J. Colloid Interface Sci.* **2017**, *490*, 314–327.

(48) Aoudjit, F.; Touahra, F.; Aoudjit, L.; Cherifi, O.; Halliche, D. Efficient solar heterogeneous photocatalytic degradation of metronidazole using heterojunction semiconductors hybrid nanocomposite, layered double hydroxides. *Water Sci. Technol.* **2020**, *82* (12), 2837–2846.

(49) Aoudjit, L.; Madjenea, F.; Lebika, H.; Sebtia, A.; Boutraa, B.; Igouda, S. Photocatalytic degradation of metronidazole using TiO$_2$ catalysts under solar irradiation. *Int. J. Chem. Environ. Eng.* **2015**, *6* (3), 150–152.

(50) Arghavan, F. S.; Al-Musawi, T. J.; Rumman, G. A.; Pelalak, R.; Khataee, A.; Nasseh, N. Photocatalytic performance of a nickel ferrite/chitosan/bismuth (III) oxyiodide nanocomposite for metronidazole degradation under simulated sunlight illumination. *J. Environ. Chem. Eng.* **2021**, *9* (4), 105619.

(51) Nasseh, N.; Taghavi, L.; Barikbin, B.; Nasseri, M. A. Synthesis and characterizations of a novel FeNi$_3$/SiO$_2$/CuS magnetic nanocomposite for photocatalytic degradation of tetracycline in simulated wastewater. *J. Clean. Prod.* **2018**, *179*, 42–54.

(52) Sohrabi, S.; Akhlaghian, F. Modeling and optimization of phenol degradation over copper-doped titanium dioxide photocatalyst using response surface methodology. *Process Saf. Environ. Prot.* **2016**, *99*, 120–128.

(53) Álvarez-Ramírez, J.; Femat, R.; Meraz, M.; Ibarra-Valdez, C. Some remarks on the Langmuir–Hinshelwood kinetics. *J. Math. Chem.* **2016**, *54* (2), 375–392.

(54) Salarian, A. A.; Hami, Z.; Mirzaei, N.; Mohseni, S. M.; Asadi, A.; Bahrami, H.; Vosoughi, M.; Alinejad, A.; Zare, M. R. N-doped TiO$_2$ nanosheets for photocatalytic degradation and

mineralization of diazinon under simulated solar irradiation: Optimization and modeling using a response surface methodology. *J. Mol. Liq.* **2016**, *220*, 183–191.

(55) Salimi, M.; Esrafili, A.; Sobhi, H. R.; Behbahani, M.; Gholami, M.; Farzadkia, M.; Jafari, A. J.; Kalantary, R. R. Photocatalytic degradation of metronidazole using D-g-C$_3$N$_4$-Bi$_5$O$_7$I composites under visible light irradiation: degradation product, and mechanisms. *ChemistrySelect* **2019**, *4* (35), 10288–10295.

(56) Du, W.; Xu, Q.; Jin, D.; Wang, X.; Shu, Y.; Kong, L.; Hu, X. Visible-light-induced photo-Fenton process for the facile degradation of metronidazole by Fe/Si codoped TiO$_2$. *RSC Adv.* **2018**, *8* (70), 40022–40034.

(57) Zhao, Z.; Fan, J.; Deng, X.; Liu, J. One-step synthesis of phosphorus-doped g-C$_3$N$_4$/Co$_3$O$_4$ quantum dots from vitamin B12 with enhanced visible-light photocatalytic activity for metronidazole degradation. *Chem. Eng. J.* **2019**, *360*, 1517–1529.

(58) Derikvandi, H.; Nezamzadeh-Ejhieh, A. Comprehensive study on enhanced photocatalytic activity of heterojunction ZnS-NiS/zeolite nanoparticles: experimental design based on response surface methodology (RSM), impedance spectroscopy and GC-MASS studies. *J. Colloid Interface Sci.* **2017**, *490*, 652–664.

(59) Fakhravar, S.; Farhadian, M.; Tangestaninejad, S. Metronidazole degradation by Z-scheme Ag$_2$S/BiVO$_4$@α-Al$_2$O$_3$ heterojunction in continuous photo-reactor: response surface methodology optimization, reaction mechanism and the effect of water matrix. *J. Environ. Chem. Eng.* **2020**, *8* (5), 104136.

(60) Bashiri, F.; Khezri, S. M.; Kalantary, R. R.; Kakavandi, B. Enhanced photocatalytic degradation of metronidazole by TiO$_2$ decorated on magnetic reduced graphene oxide:

676 Characterization, optimization and reaction mechanism studies. *J. Mol. Liq.* **2020**, *314*,
677 113608.

678 (61) Boxi, S. S.; Paria, S. Visible light induced enhanced photocatalytic degradation of organic
679 pollutants in aqueous media using Ag doped hollow TiO_2 nanospheres. *RSC Adv.* **2015**, *5*
680 (47), 37657–37668.

681 (62) Aram, M.; Farhadian, M.; Nazar, A. R. S.; Tangestaninejad, S.; Eskandari, P.; Jeon, B. H.
682 Metronidazole and Cephalexin degradation by using of $Urea/TiO_2/ZnFe_2O_4/Clinoptiloite$
683 catalyst under visible-light irradiation and ozone injection. *J. Mol. Liq.* **2020**, *304*, 112764.

684 (63) Wang, P.; Xu, S.; Wang, J.; Liu, X. Photodeposition synthesis of CdS QDs-decorated TiO_2
685 for efficient photocatalytic degradation of metronidazole under visible light. *J. Mater. Sci.:*
686 *Mater. Electron.* **2020**, *31* (22), 19797–19808.

687 (64) Li, J.; Zhao, W.; Guo, Y.; Wei, Z.; Han, M.; He, H.; Yang, S.; Sun, C. Facile synthesis and
688 high activity of novel $BiVO_4/FeVO_4$ heterojunction photocatalyst for degradation of
689 metronidazole. *Appl. Surf. Sci.* **2015**, *351*, 270–279.

690 (65) Xu, Y.; Zhang, W. D. CdS/g-C_3N_4 hybrids with improved photostability and visible light
691 photocatalytic activity. *Eur. J. Inorg. Chem.* **2015**, *2015* (10), 1744–1751.

692 (66) Hu, X.; Fan, J.; Zhang, K.; Yu, N.; Wang, J. Pharmaceuticals removal by novel nanoscale
693 photocatalyst Bi_4VO_8Cl: influencing factors, kinetics, and mechanism. *Ind. Eng. Chem.*
694 *Res.* **2014**, *53* (38), 14623–14632.

695 (67) Zhang, X.; Xie, X.; Wang, H.; Zhang, J.; Pan, B.; Xie, Y. Enhanced photoresponsive
696 ultrathin graphitic-phase C_3N_4 nanosheets for bioimaging. *J. Am. Chem. Soc.* **2013**, *135*
697 (1), 18–21.

698

699

700

701

702

703

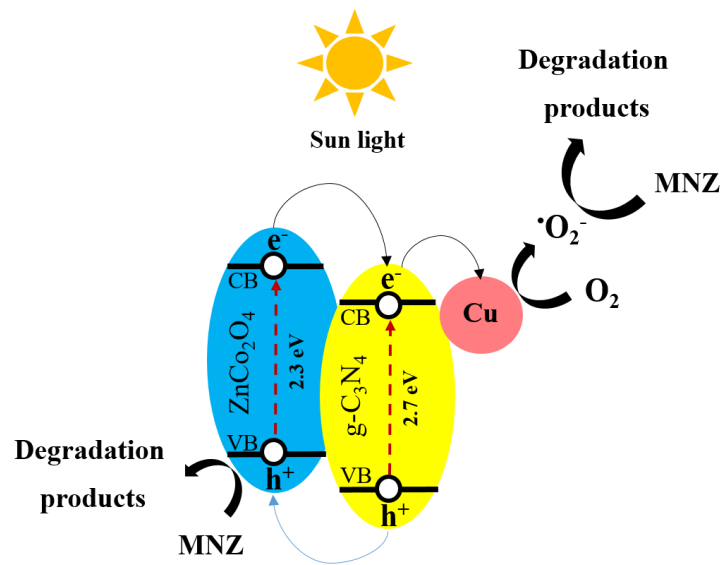704

705

706

707

708

709

710

711

712

713

714 **TOC**

715

716